Whistler Wings and Reflected Particles during Solar Wind Interaction of Lunar Magnetic Anomalies

Hui Zhang[1,2,3,4], Yong Wei[1,2,3,4], Jun Zhong[1,2,3,4], Tianxin Zhang[1,2,3,4], Libo Liu[1,2,3,4], Binbin Ni[5], Jinbin Cao[6], Song Fu[5], Yiding Chen[1,2,3,4], Suiyan Fu[7], and Weixing Wan[1,2,3,4]

1 Key Laboratory of Earth and Planetary Physics, Institute of Geology and Geophysics, Chinese Academy of Sciences, Beijing, 100029, China

2 Institutions of Earth Science, Chinese Academy of Sciences, Beijing, 100029, China

3 Beijing National Observatory of Space Environment, Institute of Geology and Geophysics, Chinese Academy of Sciences, Beijing, 100029, China

4 College of Earth Sciences, University of Chinese Academy of Sciences, Beijing, 100049, China

5 Department of Space Physics, School of Electronic Information, Wuhan University, Wuhan, China

6 School of Space and Environment, Beihang University, Beijing, 100191, China

7 School of Earth and Space Sciences, Peking University, Beijing, 100871, China

Abstract

The planetary magnetic fields in the solar system deflect/reflect solar wind at bow shocks in front of their magnetospheres, protecting the planets from direct solar wind bombardment. Indirect evidences suggest that the sporadic magnetic anomalies on the Moon, i.e., the small-scale magnetic fields, do the same, protecting the lunar surface below and even modifying the chemical/optical properties there. It is, however, still unclear how these anomalies interact with solar wind because of lack of *in-situ* observations. Two key remotely-sensed symptoms, i.e., the lunar reflected ions and the associated ~1Hz waves, are organized in a particular coordinate system here to diagnose the solar wind interaction. We show that particles are reflected around the specular direction above the lunar surface, hinting an electric-field effect in the reflection, and that whistler wings form, suggesting a distinct solar wind interaction scenario to that of a giant planetary field.

Introduction

On the Moon, despite lack of a global-scale magnetic field, many local 'magnetic anomalies' (MAs) scatter across its surface [*Purucker*, 2008]. Their sizes are typically ~100 km, comparable with the typical SW proton gyro-radii (~80 km). Their magnitudes are only several tens of nT at the lunar surface. The SW bombards and compresses the MAs, forming local magnetic structures [*Lue et al.*, 2011] which are often termed as the 'mini-magnetospheres' in the literature in order to depict a similar scenario that a magnetosphere forms on a magnetized planet. Bow shocks may also form ahead of the lunar mini-magnetospheres [*Lin et al.*, 1998]. Distinct local environment is evident on the lunar surface right beneath these mini-magnetospheres, and the surface albedo can be remarkably higher, plausibly related to the reduction of SW implantation.

The question of how SW interacts with the MAs, however, still puzzles us and we suffer mainly from lack of *in-situ* observations in the interaction region. The interaction region is most likely located at low altitudes, e.g., ~30 km [*Kurata et al.*, 2005], where satellites less enter because of the much stricter orbit controls required there to avoid the impact of satellites upon the lunar surface or mountains. Computer simulations in different plasma regimes are thus powerful to study these interactions [*Poppe et al.*, 2012; *Fatemi et al.*, 2014; *Xie et al.*, 2015; *Bamford et al.*, 2016; *Poppe et al.*, 2016]. In these simulations, the incident SW particles are seen to reflect by some specific magnetic geometries of MAs, for example, a magnetic mirror, or by the vertical ambipolar and/or Hall electric field over MAs. In the former scenario, the reflection direction depends on the geometry of the local fields, while in the latter, the specular-like reflection sounds reasonable [*Zimmerman et al.*, 2015].

The reflected particles are a critical remotely-sensed symptom to diagnose the SW-MA interaction. They have been frequently observed at ~100 km altitudes by ARTEMIS, Chang'E, SELENE(KAGUYA), and Chandrayaan-1 [*Saito et al.*, 2008; *Futaana et al.*, 2010; *Wang et al.*, 2010; *Zhong et al.*, 2013; *Harada et al.*, 2015]. A backward particle tracing technique has been facilitated to extract the reflection information from these observations. By applying this technique, *Poppe et al.* [2017] constructed a global proton reflection map of the Moon and confirmed that the reflected particles mainly originate from MAs. The reflection function was particularly investigated, and two reflection components, the isotropic function and the forward scattered Gaussian function, are found to coexist, the former dominates when the SPAB is of a low solar zenith angle while the latter dominates when the zenith angle increases. The vertical electric fields may be responsible to the reflection [*Lue et al.*, 2011; *Saito et al.*, 2012].

The reflected particles can break equilibrium of the SW plasmas surrounding the Moon and excite waves. The waves around the Moon have been observed to cover a wide frequency range. They can be 0.01 Hz ultra-low-frequency waves, ~1 Hz low-frequency whistlers, or ~1 kHz high-frequency whistlers [*Harada et al.*, 2015]. The ~1 Hz waves are very common in front of planetary bow shocks [*Narita et al.*, 2006] and they are thought to be whistler waves, which can be excited by the reflected SW ions in the foreshock [*Fairfield*, 1974; *Paschmann et al.*, 1979] or in the bow shocks [*Orlowski et al.*, 1995]. The origin of the ~1 Hz whistlers near the Moon is also on debate [*Tsugawa et al.*, 2012]. Their frequencies are as low as the ion gyro-frequency and it is reasonable to propose that they are excited by the reflected SW ions [*Nakagawa et al.*, 2011; *Tsugawa et al.*, 2012], the mismatch distributions of the reflected ions and the waves around the Moon, however, indicates that

the presence of the reflected ions is not a sufficient condition for the wave occurrence [*Harada et al.*, 2015]. The magnetic connection of the observing satellite to the lunar surface shows a good correlation with the ~1 Hz wave occurrence [*Tsugawa et al.*, 2012]. The Moon itself can act as a 'bow shock' to the incident SW, and the reflected electrons can leave away from the Moon, resonate with and thus generate the narrow-band ~100 Hz whistlers in the 'foreshock' even at a height of 1450 km [*Halekas et al.*, 2012]. The energies of the reflected electrons are up to ~100 eV and the corresponding thermal speeds can be as high as ~5000 km/s [*Halekas et al.*, 2012]. How the low-frequency broad-band whistlers generates, the frequencies of which are typically close to the gyrofrequencies of protons, however, remains unclear [*Tsugawa et al.*, 2012]. Certainly, these broad-band whistlers may not necessarily be excited at the locations where the reflected electrons arrive, but propagate to these locations after being excited just outside MAs. *Kivelson et al.* [1993] proposed that the diverted SW electrons may produce whistlers outside a small-scale magnetic obstacle. The frequencies of the whistlers are determined by the obstacle size, and they are several Hz when the obstacle size is 100-300 km in a typical SW. The whistlers propagate outward at a phase speed of ~ 500 km/s or a group speed of ~1000 km/s along magnetic field lines. A pair of whistler wings thus form in the ambient SW, and the flaring angles of the wings are ~45°.

Here, by analyzing the ARTEMIS and LP observations in a unique coordinate system (CS), we find that the low-frequency broad-band whistlers form a pair of wings beside the Moon. The mismatch of the reflected ions and the whistlers suggests that these ions aren't the wave source. These waves can be excited by electrons just outside the MAs, and the electron dynamics must play a determinative role in the SW-MA interaction.

Results

Several CSs are adopted in this study to organize satellite observations. Besides the Moon-fixed selenographic (SEL) CS and the Sun-Moon line related selenocentric solar ecliptic (SSE) CS, two specific CSs are also involved. One CS is determined by both $\boldsymbol{B}_{IMF}$ and $\boldsymbol{E}_{SW}$, and hereafter it is referred to as the 'BE' CS. Its $\boldsymbol{Y}_{BE}$ axis is always along the instantaneous interplanetary magnetic field (IMF, $\boldsymbol{B}_{IMF}$), $\boldsymbol{Z}_{BE}$ along the electric field $\boldsymbol{E}_{SW} = -\boldsymbol{V}_{SW} \times \boldsymbol{B}_{IMF}$, and $\boldsymbol{X}_{BE} = \boldsymbol{Y}_{BE} \times \boldsymbol{Z}_{BE}$. In this CS, the dayside loci where IMF lines initially touch the Moon are referred to as the 'Initially Touched Region' (ITR, with $\boldsymbol{Y}_{BE} = 0$ R_L), and the rest downstream lunar surface is termed as the 'Field Connected Region' (FCR). The head-on SW bombardment occurs in ITR only when $\theta_{SW-IMF} = \cos^{-1}(\boldsymbol{V}_{SW} \cdot \boldsymbol{B}_{IMF}/(|\boldsymbol{V}_{SW}||\boldsymbol{B}_{IMF}|))$ is close to 90º. If necessary, another CS, denoted as the 'VE' CS, is used. $\boldsymbol{X}_{VE}$ axis is always against the instantaneous $-\boldsymbol{V}_{SW}$, $\boldsymbol{Z}_{VE}$ along $\boldsymbol{E}_{SW}$, and $\boldsymbol{Y}_{VE} = \boldsymbol{Z}_{VE} \times \boldsymbol{X}_{VE}$. Here, $\boldsymbol{V}_{SW}$ and $\boldsymbol{B}_{IMF}$ are obtained from the NASA/Goddard Space Flight Center (GSFC)'s OMNI data set and are further shifted forward or backward to the Moon.

To examine the spatial distributions of the low-frequency broad-band waves around the Moon, the magnetic field observations from 1998 to 1999 by a low-altitude (20-120 km) Lunar Prospector (LP) mission [*Walker and Russell*, 2013] are analyzed in Fig. 1. The root mean square (RMS) in a 5-second window of the magnetic fields observed by LP at a temporal resolution of 1/9 second is used to quantify the magnitude of the whistlers [*Halekas et al.*, 2006]. The spherical distributions of the RMS around the Moon are unfolded by the zenith angles relative to the X axes of the aforementioned four CSs in Fig. 1b-f. For comparison, the distributions of the modeled lunar crustal fields at the 10 km altitude over the lunar surface [*Purucker*, 2008] is also shown in Fig. 1a in SEL. A big MA is clearly seen on the southern far-side, coincident with the position of the SPAB. When

120 the Moon is immersed inside the supersonic SW (the geocentric solar zenith angle of the Moon is
121 less than 135°, Fig. 1b), the strong waves are observed closely related to the SPAB MA. These
122 waves disappear, however, when the Moon is located inside the subsonic
123 magnetosphere/magnetosheath (the geocentric solar zenith angle is greater than 135°, Fig. 1c). The
124 waves in Fig. 1b are relocated in SSE as shown in Fig. 1d, and they show up only on the dayside
125 and mainly in the southern hemisphere where the SPAB is located. All these observations indicate
126 the waves are the consequence of the SW interaction of MAs. The wave activities scatter all across
127 the dayside in the VE CS (Fig. 1e) and no special pattern is presented related to $\boldsymbol{Z}_{VE}$ i.e., to $\boldsymbol{E}_{SW}$.
128 In BE, however, the waves are well structured (Fig. 1f) and they do not appear near the ITR (the
129 dark blue band in the center of Fig. 1f), at least at the LP heights of 20-120 km. Still, no asymmetric
130 features is seen along $\boldsymbol{Z}_{BE}$ or $\boldsymbol{E}_{SW}$ in Fig. 1f, which would have been observed if the waves were
131 produced by the reflected particles since $\boldsymbol{E}_{SW}$ must have made an asymmetric distribution of these
132 particles [*Harada et al.*, 2015; *Zhang et al.*, 2020].
133
134 The waves observed by ARTEMIS, as well as by LP, are examined statistically in Fig. 2 from
135 another perspective, i.e., in the XY plane of the BE CS, which is perpendicular to $\boldsymbol{E}_{SW}$. The
136 ARTEMIS satellite orbits are higher than 100 km. The plasma data collected by the ESA instrument
137 and the magnetic field data by the SCM instrument from the middle of 2011 to the middle of 2016
138 are used here [*Angelopoulos*, 2011; *McFadden et al.*, 2008; *Roux et al.*, 2008]. The observations
139 confined within the scope of $|\boldsymbol{Z}_{BE}| < 0.5\ R_L$ and $120\ km < \sqrt{\boldsymbol{X}_{BE}^2 + \boldsymbol{Y}_{BE}^2} - R_L < R_L$ are adopted
140 in this Figure. Similar with the LP case, the RMS of the SCM data within 5-second sliding windows
141 with a temporal resolution of 0.125 second is used to quantify the wave activities. The left three
142 columns in Fig 2 show the XY plane projections of the waves observed by LP at low altitudes (Fig.

2, a-c: 20-60 km; a'-c': 60-120 km) and by ARTEMIS at high altitudes (Fig. 2, a"-c": 120 km-1 R_L) as a function of height (in columns) and θ_{SW-IMF} (in rows). Since $\boldsymbol{E}_{SW}$ does not control the wave distribution pattern as seen in Fig. 1e and 1f, when θ_{SW-IMF} of a data point is greater than 90°, the signs of the X_{BE} and Z_{BE} coordinates of all the vectors of this data point are reversed. In this case, $\boldsymbol{E}_{SW}$ points along $-\boldsymbol{Z}_{BE}$, $\boldsymbol{B}_{IMF}$ along $-\boldsymbol{Y}_{BE}$, and $\boldsymbol{V}_{SW}$ always in the direction of $-\boldsymbol{X}_{BE}$ and $+\boldsymbol{Y}_{BE}$ as shown in Fig. 2.

There are clear patterns shown for the wave-occupied regions as well as for the wave-absent regions in Fig 2. The low-frequency wave regions are rooted at the whole dayside region near the lunar surface except for the ITR. The wave regions expand outward along the background IMF, forming a pair of wings beside the ITR. The flaring angle seems to vary with θ_{SW-IMF}, and from Fig. 2a" to Fig. 2c" it increases from ~65° (Fig. 2a", $\theta_{SW-IMF} \in [72°, 108°]$), via ~75° (Fig. 2b", $\theta_{SW-IMF} \in [36°, 72°]$ or $[108°, 144°]$), to ~90° (Fig. 2c", $\theta_{SW-IMF} < 36°$ or $> 144°$). The two wings are pretty asymmetric about the $\boldsymbol{Y}_{BE} = 0$ plane for the oblique case, and the wing is much smaller at the side near the lunar wake. At the IMF lines connecting to the nightside surface or to the wake, the waves cannot appear in the regions very close to the lunar surface or the wake, forming a wave absent cone behind the Moon with a flaring angle ~45°. This pattern is particularly very clear for the quasi-perpendicular case in Fig. 2a", and the scale of the wings in the $\boldsymbol{X}_{BE}$ dimension is about 1 R_L, which is a little bit larger at the outer portion of the wings. These observations suggest that neither the wake nor the nightside lunar surface are the source region.

The waves are observed to be all absent in the region around the ITR. The angular width of this dayside wave absent region is observed to be controlled both by satellite altitude and θ_{SW-IMF}. If

comparing the ITR wave absent regions in a row in Fig 2, we will see that the angular width increases as the observing altitude increases. If comparing them in a column, we will see that the ITR wave absent region shrinks when $\boldsymbol{B}_{IMF}$ and $\boldsymbol{V}_{SW}$ tend to be parallel or antiparallel.

The wave absence near the ITR may hint some particular behaviors of the reflection SW if these ions can excite the waves. ARTEMIS satellites provide a full distribution of protons in the phase space at a resolution of ~4 seconds [*McFadden et al.*, 2008]. To make it simple, the protons distributed within a 45º cone on the opposite side to the Sun are considered as the incident SW particles, while those outside the cone are taken as the lunar reflected particles [*Harada et al.*, 2015]. The densities of the incident SW (N_{SW}) and the reflected SW (N_{RF}) can be calculated, respectively. The distributions of the normalized density of the reflected protons (N_{RF}/N_{SW}) are shown in the right column of Fig. 2. It is clearly seen that the reflected ions can occur all over the dayside lunar surface, not only in FCR but also in ITR. For the quasi-perpendicular case (Fig. 2a*), the reflected protons are observed to be able to traverse $\boldsymbol{B}_{IMF}$ and reach a height up to ~400 km. For the quasi-parallel case (Fig. 2c*), the reflected protons can move upward along the IMF reaching the much higher altitudes up to 1 R_L. The presence of the reflected protons and the disappearance of the waves in the ITR may also suggest that the reflected SW particles are not the source for the waves, unless some peculiar behavior occurs there for the reflected SW which can suppress the waves.

In fact, the XY plane of the BE CS is convenient for examining the reflected properties, particularly because this plane is always perpendicular to $\boldsymbol{E}_{SW}$ and $\boldsymbol{V}_{Y,BE}$ of a reflected proton remained unchanged even at a high altitude. The XY projections of the distributions of the outward-going reflected protons in ITR are examined in the phase space in the modified BE CS as shown in Fig. 3.

All the reflected protons involved are observed by the ESA instrument when the ARTEMIS satellites are located within 5° separated from the $Y_{BE} = 0$ plane (ITR) and at the altitudes from 50 km to 400 km. The three columns in Fig. 3 show the original phase space density (PSD), the normalized PSD by the maximum SW PSD and the occurrence probability density of reflected protons in the phase space. It is seen that the reflected protons occur mainly at energies beyond 500 eV and exhibit a broad specular reflection for all the three θ_{SW-IMF} cases, or, let's say, a forward scattered Gaussian reflection [*Poppe et al.*, 2017]. The lower-energy protons (<100 eV) exhibit a diffuse reflection. Although their PSD is high, the number density of the low-energy protons should be low since the corresponding volume in the phase space is very much smaller than that of the high-energy protons. That is why the occurrence probability for the low-energy protons is low in Fig. 3a"-3c". In addition, satellite altitude seems not to control the distribution functions.

Discussion

The low-frequency broad-band whistlers near the Moon have the frequencies from 0.1 to 10 Hz, close to the SW proton gyro-frequency (~0.1 Hz) but lower than the electron gyro-frequency (200 Hz). This frequency match, as well as, the fact that the whistlers are often observed to cooccur with the reflected protons, make it possible that the reflected ions are the wave source [*Nakagawa et al.*, 2011; *Tsugawa et al.*, 2012]. *Harada et al.* [2015] has shown, however, that at the lunar flank which $\boldsymbol{E}_{SW}$ points to, the waves cannot be detected. In this study, the waves are also observed to disappear in the ITR, where, however, the reflected protons can exist. All these observations suggest that the presence of the reflected ions is not a sufficient condition for the wave occurrence [*Harada et al.*, 2015]. The magnetic connection of the observing satellite to the lunar surface shows a good correlation with the ~1 Hz wave occurrence [*Tsugawa et al.*, 2012], which makes it possible that the

electrons reflected on the lunar surface or MAs can resonate with and thus maintain whistlers along their tracks [*Halekas et al.*, 2012]. In this way, the high-frequency (~100 Hz) narrow-band whistlers are well-understood, the low-frequency broad-band ones, however, seem not. The energies of the resonating electrons can be as high as ~100 eV, and the corresponding thermal velocities are about 5000 km/s. If these electrons excite the low-frequency whistlers, the flaring angle of the whistler wings should be almost 90 º since the thermal velocities of the electrons are much faster than $\boldsymbol{V}_{SW}$.

The low-frequency whistlers have been proposed to be excited by the diverted electron fluid just outside a magnetic obstacle of the size less than the gyro-radii of SW protons [*Kivelson et al.*, 1993]. These whistlers may propagate outward from the interaction region along IMF in the rest frame of SW, occupy the entire upstream region when $\theta_{SW-IMF}\sim 0°$ or $180°$, or form a pair of whistler wings behind when $\theta_{SW-IMF}\sim 90°$ [*Gurnett*, 1995]. That is exactly what we see at the Moon. At the altitudes of ARTEMIS, for any θ_{SW-IMF}, the waves are observed to form whistler wings. The flaring angle of the wings is about 70º When $\theta_{SW-IMF}\sim 90°$. The corresponding field-aligned propagating velocity, $\boldsymbol{V}_W$, of the waves can be estimated to be ~1000 km/s, given the perpendicular component of $\boldsymbol{V}_{SW}$, $\boldsymbol{V}_C$, of ~400 km/s. When $\boldsymbol{V}_{SW}$ is parallel/anti-parallel to $\boldsymbol{B}_{IMF}$, the wings change to be asymmetric, the wings become more flaring and the waves can occupy the upstream region against the incident SW because of their fast speed. At the altitudes of LP, it is seen that the wave-absent region around ITR shrinks when θ_{SW-IMF} decreases or when the height decreases.

The whistlers are possibly able to excite in ITR at a height of ~30 km of the interaction region [*Kurata et al.*, 2005], lower than both LP or ARTEMIS as schematically shown in Fig. 4. After generation, they propagate at a velocity of $\boldsymbol{V}_W$ along $\boldsymbol{B}_{IMF}$ from the low-altitude interaction

region and convect at a velocity of $\boldsymbol{V}_C$ with the background SW, forming whistler wings as shown by the pink dot lines in Fig. 4. Because $\boldsymbol{V}_W$ is ~1000 km/s, much larger than $\boldsymbol{V}_C$ (<400 km/s), the flaring angle, $\tan^{-1}|\boldsymbol{V}_W|/|\boldsymbol{V}_C|$, is thus as large as 70°. The wings open widely into the nearby space and may not encounter the lunar surface. The higher the satellite orbit, the wider the wave-absent region along the satellite orbit will be, as shown by the black portions along the two satellite trajectories in Fig. 4. When θ_{SW-IMF} decreases, $\boldsymbol{V}_C$ will decrease, thereby increasing the flaring angle of the wings and narrowing the wave-absent region along the satellite orbit. The interacting MAs are not necessarily located in the ITR as depicted in Fig. 4. If the MAs are located in the FCR, one wing will encounter the lunar surface and disappear and the other one maintains. Statistically they can still result in the distribution pattern as shown in Fig. 2. In this scenario, certainly, no asymmetric features can be expected related to $\boldsymbol{E}_{SW}$, as shown in Fig. 1f.

The wave properties are also understood in this scenario. *Kivelson et al.* [1993] proposed that the wave power peaks at wavelengths comparable with the transverse scale of the magnetic obstacle. In the lunar case, the scale may majorly be determined by the horizontal scales of the MAs, which are several hundreds of kilometers. According to the dispersion relation and the SW properties at the lunar orbit, the wave frequency should be ~1 Hz and the group velocity be ~1000 km/s. The magnetic fields of an MA on the Moon are never able to be described by a simple dipole field, their magnitude, geometry and dimensions vary a lot [*Purucker*, 2008]. Since the obstacle size is critical to determine wave properties, the broad-band frequencies of the lunar whistlers may derive from the complicity of the magnetic fields over the lunar surface.

Finally, it should be mentioned that the BE CS adopted in this study is convenient for the study of reflected protons. In the ITR, the reflected protons are observed to reach the height up to ~400 km across $\boldsymbol{B}_{IMF}$, and the initial reflection velocity can be inferred. Given $\boldsymbol{B}_{IMF} = 10\ nT$, the 400 km gyro-radius corresponds to a reflected proton velocity of ~380 km/s and a reflection energy of ~800 eV, which is consistent with that shown in Fig. 3. That the reflection velocity is about 0.8 of the SW velocity magnitude sounds appropriate [*Holmstrom et al.*, 2010; *Saito et al.*, 2008]. The reflection function has been carefully investigated by *Saito et al.* [2008] and *Poppe et al.* [2017]. The phase space distribution functions of the reflected protons investigated in this study show that the high-energy protons (>500 eV) experience a specular-like or forward scattered Gaussian reflection [*Poppe et al.*, 2017] and that the reflection of low-energy protons seems diffuse. The electric fields over MAs seem to play a significant role in reflecting protons [*Lue et al.*, 2011; *Saito et al.*, 2012; *Zimmerman et al.*, 2015]. Although they may not produce the whistlers around the ITR, the effect of these reflected protons may be further investigated.

Acknowledgement

This work was supported by the B-type Strategic Priority Program of the Chinese Academy of Sciences, Grant No. XDB41000000 and the National Natural Science Foundation of China (41731068, 41774175, 41941001, 41674163, and 41974186). The authors thank the PPI Node of the PDS at UCLA: https://pds-ppi.igpp.ucla.edu for providing the magnetic field observations from the Lunar Prospector mission, thank the NASA/GSFC's Space Physics Data Facility for the OMNI Web service at http://cdaweb.gsfc.nasa.gov for providing the solar wind and the interplanetary magnetic field data. We acknowledge NASA contract NAS5-02099 and V. Angelopoulos for use of data from the THEMIS Mission, and specifically, acknowledge O. LeContel and the late A. Roux

for use of SCM data and C. W. Carlson and J. P. McFadden for use of ESA data. Both the SCM and ESA data of ARTEMIS are obtained from http://themis.igpp.ucla.edu. The authors are especially grateful to Dr. Krishan K. Khurana of UCLA for his insightful and useful suggestions to this work.

References

Angelopoulos, V. (2011), The ARTEMIS mission, *Space Science Reviews*, *165*(1-4), 3-25, doi:10.1007/s11214-010-9687-2.

Bamford, R. A., et al. (2016), 3D PIC simulations of collisionless shocks at lunar magnetic anomalies and their role in forming lunar swirls, *Astrophys. J.*, *830*(2), 12, doi:10.3847/0004-637x/830/2/146.

Fairfield, D. H. (1974), Whistler waves observed upstream from collisionless shocks, *Journal of Geophysical Research*, *79*(10), 1368-1378, doi:10.1029/JA079i010p01368.

Fatemi, S., M. Holmstrom, Y. Futaana, C. Lue, M. R. Collier, S. Barabash, and G. Stenberg (2014), Effects of protons reflected by lunar crustalmagnetic fields on the global lunar plasma environment, *J. Geophys. Res-Space Phys.*, *119*(8), doi:10.1002/2014ja019900.

Futaana, Y., S. Barabash, M. Wieser, M. Holmstrom, A. Bhardwaj, M. B. Dhanya, R. Sridharan, P. Wurz, A. Schaufelberger, and K. Asamura (2010), Protons in the near-lunar wake observed by the Sub-keV Atom Reflection Analyzer on board Chandrayaan-1, *J. Geophys. Res-Space Phys.*, *115*, doi:10.1029/2010ja015264.

Gurnett, D. A. (1995), The whistler-mode bow wave of an asteroid, *J. Geophys. Res-Space Phys.*, *100*(A11), 21623-21629, doi:10.1029/95ja02225.

Halekas, J. S., D. A. Brain, D. L. Mitchell, and R. P. Lin (2006), Whistler waves observed near lunar crustal magnetic sources, *Geophys. Res. Lett.*, *33*(22), doi:10.1029/2006gl027684.

Halekas, J. S., A. Poppe, G. T. Delory, W. M. Farrell, and M. Horanyi (2012), Solar wind electron interaction with the dayside lunar surface and crustal magnetic fields: Evidence for precursor effects, *Earth Planets Space*, *64*(2), 73-82, doi:10.5047/eps.2011.03.008.

Harada, Y., J. S. Halekas, A. R. Poppe, Y. Tsugawa, S. Kurita, and J. P. McFadden (2015), Statistical characterization of the foremoon particle and wave morphology: ARTEMIS observations, *J. Geophys. Res-Space Phys.*, *120*(6), 4907-4921, doi:10.1002/2015ja021211.

Holmstrom, M., M. Wieser, S. Barabash, Y. Futaana, and A. Bhardwaj (2010), Dynamics of solar wind protons reflected by the Moon, *J. Geophys. Res-Space Phys.*, *115*, 8, doi:10.1029/2009ja014843.

Kivelson, M. G., L. F. Bargatze, K. K. Khurana, D. J. Southwood, R. J. Walker, and P. J. Coleman (1993), Magnetic-field signatures near Galileo closest approach to Gaspra, *Science*, *261*(5119), 331-334, doi:10.1126/science.261.5119.331.

Kurata, M., H. Tsunakawa, Y. Saito, H. Shibuya, M. Matsushima, and H. Shimizu (2005), Mini-magnetosphere over the Reiner Gamma magnetic anomaly region on the Moon, *Geophys. Res. Lett.*, *32*(24), doi:10.1029/2005gl024097.

Lin, R. P., D. L. Mitchell, D. W. Curtis, K. A. Anderson, C. W. Carlson, J. McFadden, M. H. Acuna, L. L. Hood, and A. Binder (1998), Lunar surface magnetic fields and their interaction with the solar wind: Results from lunar prospector, *Science*, *281*(5382), 1480-1484, doi:10.1126/science.281.5382.1480.

Lue, C., Y. Futaana, S. Barabash, M. Wieser, M. Holmström, A. Bhardwaj, M. B. Dhanya, and P. Wurz (2011), Strong influence of lunar crustal fields on the solar wind flow, *Geophys. Res. Lett.*, *38*(3), doi:10.1029/2010gl046215.

McFadden, J. P., C. W. Carlson, D. Larson, M. Ludlam, R. Abiad, B. Elliott, P. Turin, M. Marckwordt, and V. Angelopoulos (2008), The THEMIS ESA plasma instrument and in-flight calibration, *Space Science Reviews*, *141*(1-4), 277-302, doi:10.1007/s11214-008-9440-2.

Nakagawa, T., F. Takahashi, H. Tsunakawa, H. Shibuya, H. Shimizu, and M. Matsushima (2011), Non-monochromatic whistler waves detected by Kaguya on the dayside surface of the moon, *Earth Planets Space*, *63*(1), 37-46, doi:10.5047/eps.2010.01.005.

Narita, Y., K. H. Glassmeier, K. H. Fornacon, I. Richter, S. Schafer, U. Motschmann, I. Dandouras, H. Reme, and E. Georgescu (2006), Low-frequency wave characteristics in the upstream and downstream regime of the terrestrial bow shock, *J. Geophys. Res-Space Phys.*, *111*(A1), doi:10.1029/2005ja011231.

Orlowski, D. S., C. T. Russell, D. Kraussvarban, N. Omidi, and M. F. Thomsen (1995), DAMPING AND SPECTRAL FORMATION OF UPSTREAM WHISTLERS, *J. Geophys. Res-Space Phys.*, *100*(A9), 17117-17128, doi:10.1029/95ja00062.

Paschmann, G., N. Sckopke, S. J. Bame, J. R. Asbridge, J. T. Gosling, C. T. Russell, and E. W. Greenstadt (1979), Association of low-frequency waves with suprathermal ions in the upstream solar-wind, *Geophys. Res. Lett.*, *6*(3), 209-212, doi:10.1029/GL006i003p00209.

Poppe, A. R., S. Fatemi, I. Garrick-Bethell, D. Hemingway, and M. Holmstrom (2016), Solar wind interaction with the Reiner Gamma crustal magnetic anomaly: Connecting source magnetization to surface weathering, *Icarus*, *266*, 261-266, doi:10.1016/j.icarus.2015.11.005.

Poppe, A. R., J. S. Halekas, G. T. Delory, and W. M. Farrell (2012), Particle-in-cell simulations of the solar wind interaction with lunar crustal magnetic anomalies: Magnetic cusp regions, *J. Geophys. Res-Space Phys.*, *117*, 16, doi:10.1029/2012ja017844.

Poppe, A. R., J. S. Halekas, C. Lue, and S. Fatemi (2017), ARTEMIS observations of the solar wind proton scattering function from lunar crustal magnetic anomalies, *J. Geophys. Res.-Planets*, *122*(4), 771-783, doi:10.1002/2017je005313.

Purucker, M. E. (2008), A global model of the internal magnetic field of the Moon based on Lunar Prospector magnetometer observations, *Icarus*, *197*(1), 19-23, doi:10.1016/j.icarus.2008.03.016.

Roux, A., O. Le Contel, C. Coillot, A. Bouabdellah, B. de la Porte, D. Alison, S. Ruocco, and M. C. Vassal (2008), The Search Coil Magnetometer for THEMIS, *Space Science Reviews*, *141*(1-4), 265-275, doi:10.1007/s11214-008-9455-8.

Saito, Y., M. N. Nishino, M. Fujimoto, T. Yamamoto, S. Yokota, H. Tsunakawa, H. Shibuya, M. Matsushima, H. Shimizu, and F. Takahashi (2012), Simultaneous observation of the electron acceleration and ion deceleration over lunar magnetic anomalies, *Earth Planets Space*, *64*(2), 83-92, doi:10.5047/eps.2011.07.011.

Saito, Y., et al. (2008), Solar wind proton reflection at the lunar surface: Low energy ion measurement by MAP-PACE onboard SELENE (KAGUYA), *Geophys. Res. Lett.*, *35*(24), doi:10.1029/2008gl036077.

Tsugawa, Y., et al. (2012), Statistical study of broadband whistler-mode waves detected by Kaguya near the Moon, *Geophys. Res. Lett.*, *39*(16), doi:https://doi.org/10.1029/2012GL052818.

Walker, R. J., and C. T. Russell (2013), Magnetic field data from the Lunar Prospector Magnetometer, *NASA Planetary Data System, LP-L-MAG-4-SUMM-LUNARCRDS-5SEC-V1.0*.

Wang, X. D., et al. (2010), Acceleration of scattered solar wind protons at the polar terminator of the Moon: Results from Chang'E-1/SWIDs, *Geophys. Res. Lett.*, *37*, doi:10.1029/2010gl042891.

Xie, L. H., L. Li, Y. T. Zhang, Y. Y. Feng, X. Y. Wang, A. B. Zhang, and L. G. Kong (2015), Three-dimensional Hall MHD simulation of lunar minimagnetosphere: General characteristics and comparison with Chang'E-2 observations, *J. Geophys. Res-Space Phys.*, *120*(8), 6559-6568, doi:10.1002/2015ja021647.

Zhang, T.-X., et al. (2020), Asymmetric Lunar Magnetic Perturbations Produced by Reflected Solar Wind Particles, *Astrophys. J. Lett.*, *893*(2), doi:10.3847/2041-8213/ab8640.

374 Zhong, J., et al. (2013), Chang'E-1 observations of pickup ions near the Moon under different
375 interplanetary magnetic field conditions, *Planet Space Sci.*, *79-80*, 56-63,
376 doi:10.1016/j.pss.2013.02.001.
377 Zimmerman, M. I., W. M. Farrell, and A. R. Poppe (2015), Kinetic simulations of kilometer-scale
378 minimagnetosphere formation on the Moon, *J. Geophys. Res.-Planets*, *120*(11), 1893-1903,
379 doi:10.1002/2015je004865.

380

Figures:

Fig. 1. The spherical distributions of the modeled lunar crustal magnetic field and the low-frequency waves near the Moon. The distributions are unfolded to the YZ planes in different CSs by the zenith angles relative to their X axes. a) The modeled crustal magnetic fields at the altitude of 10 km in the SEL CS. b-f) the magnetic field RMS observed by the Lunar Prospector. b and c) the wave activities in the SEL when the Moon is in the SW and in the magnetosphere, respectively. d-f) the wave activities distributed in the SSE, VE and BE CSs, respectively when the Moon is located in the SW. Data in Panels b, d, e and f are the same but they exhibit different patterns.

Fig. 2. The XY-plane projections of the distributions of the low-frequency waves and the reflected SW protons. The plots in a column are shown as a function of θ_{SW-IMF}. a-c and a'-c' are the magnetic field RMS observed by LP at 30-60 km and at 60-120 km, respectively. a"-c" are the RMS observed by ARTEMIS from 120 km to 1 R_L. a*-c* show the normalized densities of the reflected protons.

Fig. 3. The XY-plane projections the phase-space distributions of the outward-going reflected protons in the ITR below 400 km in the modified BE CS. Three columns show the original phase space density (PSD), the normalized PSD and the occurrence probability density of the reflected protons, respectively, and the rows are organized by θ_{SW-IMF}.

Fig. 4. The propagation scenario of the low frequency whistlers. The waves are excited over an MA in the ITR (the red arch) below the observing satellite. The whistlers propagate at $\boldsymbol{V}_W$ along $\boldsymbol{B}_{IMF}$

405 away from the interaction region and move at $\boldsymbol{V}_C$ together with SW, forming whistler wings (the
406 pink dot lines). The waves can never show up in the portion of the satellite trajectory outside the
407 wings.

Figure 1.

a.
ZSEL
YSEL
XSEL
90
180
b.
ZSEL
YSEL
XSEL
90
180
c.
ZSEL
YSEL
XSEL
90
180
d.
ZSSE
YSSE
XSSE
90
180
e.
ZVE
ESW
YVE
−VSW
XVE
90
180
f.
ZBE
YBE
B
XBE
90
180
B RMS (nT)
0.6
0.4
0.2
0.0
Model B (nT)
9
6
3
0

Figure 2.

LP B RMS (nT)

0.0 0.2 0.4 0.6

LP B RMS (nT)

0.0 0.2 0.4 0.6

ARTEMIS B RMS (nT)

0.0 0.1 0.2 0.3

NRF/NSW

0.00 0.02 0.04

a a' a'' a*

b b' b'' b*

c c' c'' c*

IMF

Vsw

X_{BE} (R_L)

Y_{BE} (R_L)

2 1 0 −1 −2

Figure 3.

log10(PSD)

−18 −16 −14 −12 −10 −8

log10(PSD/max(PSD))

−12 −10 −8 −6 −4 −2

log10(Probability Density)

−5.0 −4.5 −4.0 −3.5 −3.0 −2.5 −2.0

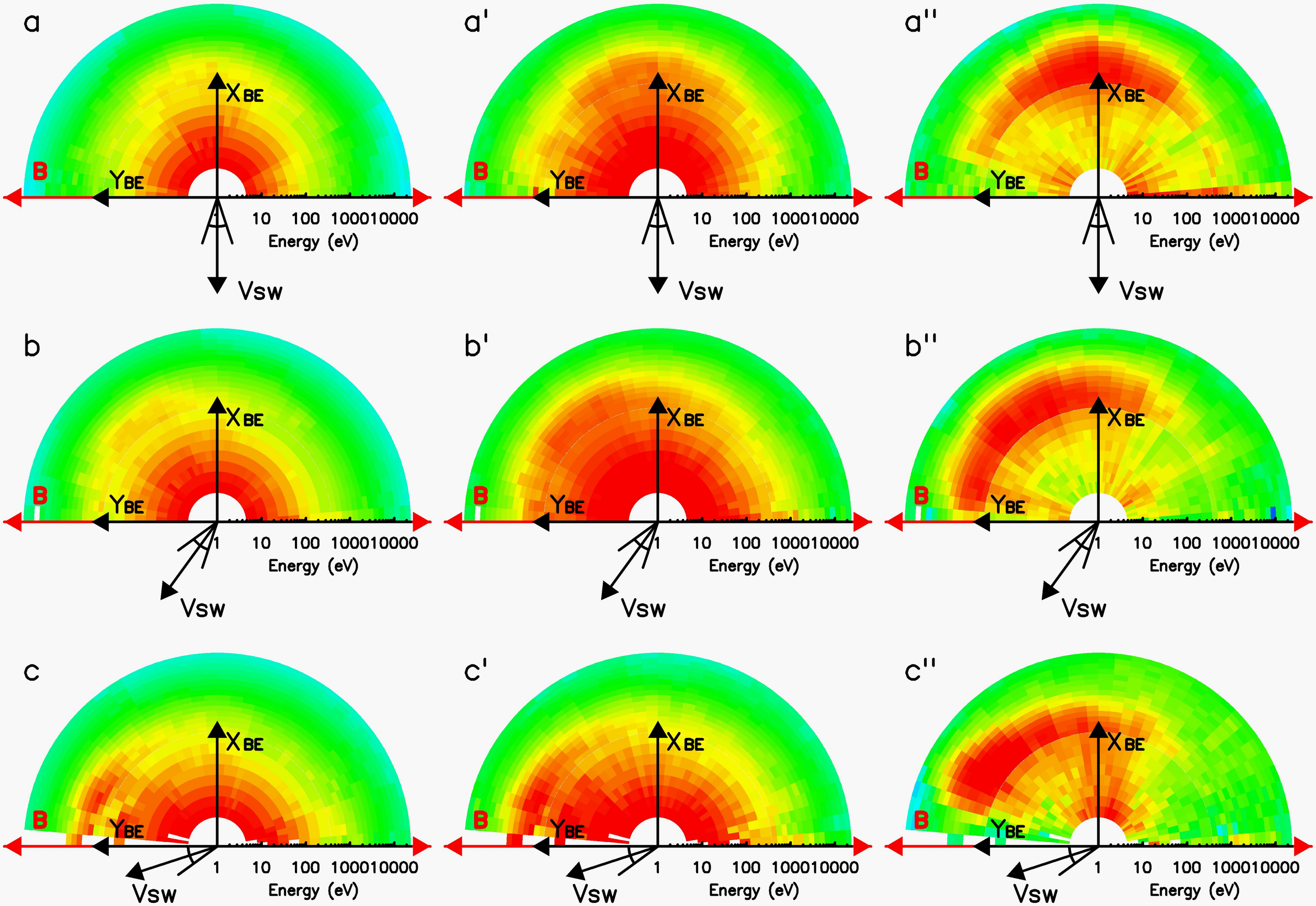

Figure 4.

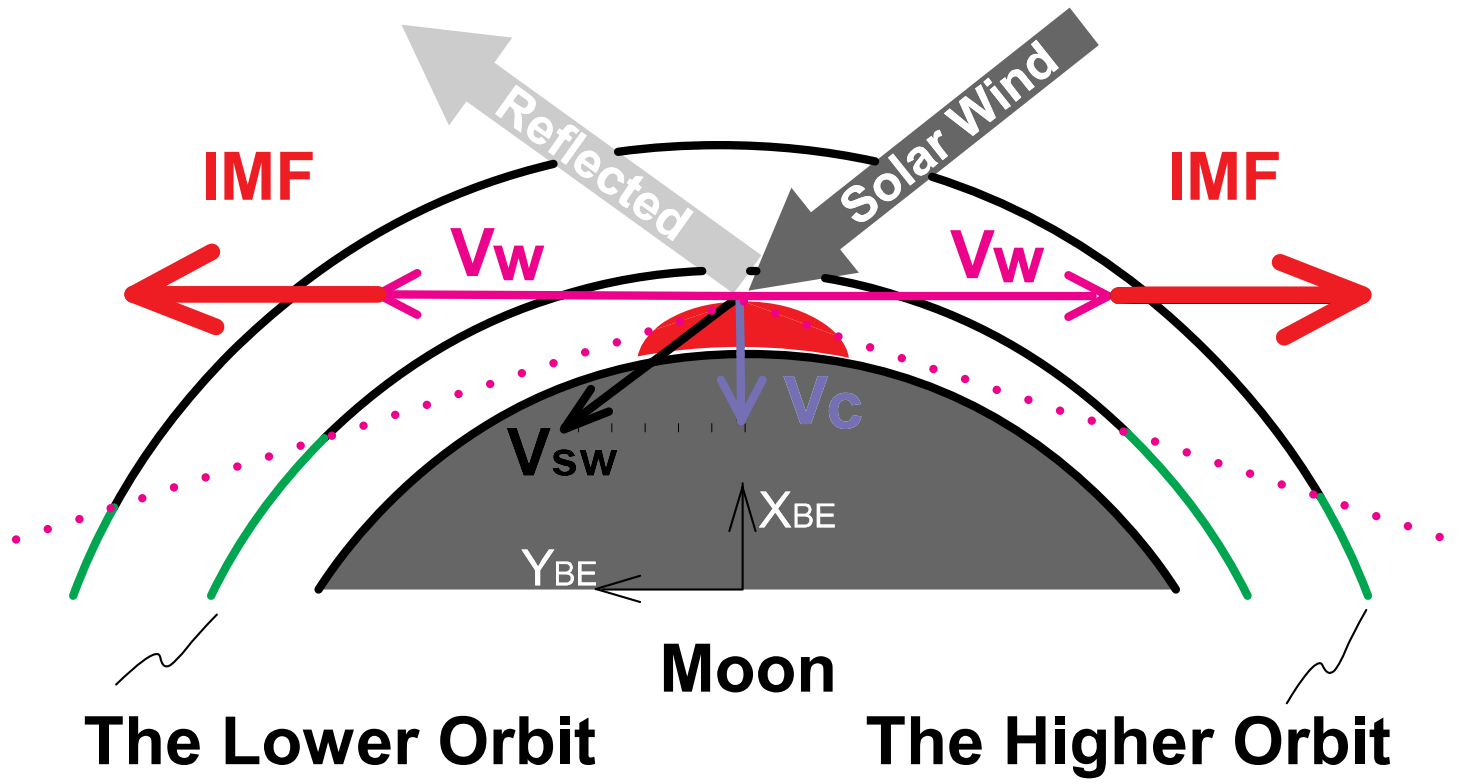
Reflected
Solar Wind
IMF
IMF
Vw
Vw
Vc
Vsw
XBE
YBE
Moon
The Lower Orbit
The Higher Orbit